InP-Based Waveguide-Integrated Photodiodes With InGaAs/GaAsSb Type-II Quantum Wells and 10-GHz Bandwidth at 2 μm Wavelength

Bassem Tossoun ⬡, Jizhao Zang ⬡, Sadhvikas J. Addamane, Ganesh Balakrishnan, *Senior Member, IEEE*, Archie L. Holmes, Jr., *Senior Member, IEEE*, and Andreas Beling ⬡, *Senior Member, IEEE*

Abstract—Waveguide-integrated photodiodes with InGaAs/ GaAsSb type-II quantum well absorption regions designed to absorb light at 2 μm are presented. A novel dual-integrated waveguide-depletion layer was used to maximize quantum efficiency in photodiodes designed with thin absorbers for high-speed optical response. Low dark currents (1 nA at -1 V) and an internal responsivity of 0.84 A/W along with a bandwidth above 10 GHz and an open eye diagram at 10 Gb/s have been demonstrated at 2 μm. The high-speed carrier dynamics within InGaAs/GaAsSb type-II quantum wells are explored for the first time and suggest that the transit time of the photodiode is limited by light hole escape times in the quantum wells.

Index Terms—InP, MWIR, photodetectors, photodiodes, photonic integrated circuits (PICs), SWIR, waveguides.

I. INTRODUCTION

THE 2 μm wavelength region has gained significant interest for its potential application in next-generation optical communications networks [1]. Most of the components required to build components and photonic integrated circuits (PICs) operating at 2 μm such as semiconductor lasers, optical amplifiers, and arrayed waveguide gratings have already been developed [2]. And, with the progress of hollow core photonic bandgap fibers (HC-PBGF), WDM transmission at 2 μm with losses of less than 0.2 dB/km have been demonstrated [3]. Furthermore, it is well known that high-speed photodetectors with high optoelectronic (O/E) conversion efficiency are essential components for future optical communications systems. However, only few semiconductor high-speed photodetectors and waveguide photodiodes have been developed extensively for 2 μm to date [4]–[7].

B. Tossoun, J. Zang, A. L. Holmes, Jr., and A. Beling are with the Charles L. Brown Department of Electrical and Computer Engineering, University of Virginia, Charlottesville, VA 22901 USA (e-mail: bmt3av@virginia.edu; jz4nd@virginia.edu; ah7sj@virginia.edu; ab3pj@eservices.virginia.edu).

S. J. Addamane and G. Balakrishnan are with the Department of Electrical and Computer Engineering, University of New Mexico, Albuquerque, NM 87106 USA (e-mail: addamane@unm.edu; gunny@unm.edu).

Color versions of one or more of the figures in this paper are available online at http://ieeexplore.ieee.org.

Photodetectors for 2 μm are also useful for gas and chemical sensing, LIDAR, and medical applications. The 2 μm wavelength region offers an "eye safe" platform for coherent LIDAR systems employed by self-driving cars to sense obstacles and avoid collisions [8]. Additionally, CO_2 gases in the atmosphere can be sensed at 2 μm, which is helpful in tracking global climate change [9]. Also, given that water absorbs at around 2 μm, detectors can also be used to monitor blood glucose levels in diabetics.

In the past, waveguide-integrated photodiodes (PDs) based on multiple InGaAs/GaAsSb type-II quantum wells (MQW) have shown promise of high-speed detection at 2 μm [11]. These photodiodes are grown lattice-matched on indium phosphide (InP), a well established platform for PICs, that offers the advantage of complex bandgap engineering of active devices. Through optimization of the quantum well layers, and the addition of a novel dual-integrated waveguide-depletion layer, significant improvements in dark current (1 nA at -1 V), internal responsivity (0.84 A/W) and bandwidth ($>$ 10 GHz) at 2 μm are demonstrated in this paper. Experimental data on the static and high-frequency O/E characteristics are studied and supported by device modeling and optical simulations.

II. DEVICE DESIGN AND FABRICATION

A. Design and Simulation

Three different photodiode structures were grown by molecular beam epitaxy (MBE) on semi-insulating InP substrate and are schematically shown in Fig. 1. Sample A is a p-i-n photodiode with an integrated rib waveguide on which we have previously reported [11]. Samples B and C are similar to a dual-depletion layer photodiode, with a depleted absorption layer consisting of MQWs and an optically transparent electron collection layer to minimize capacitance while simultaneously reducing carrier transit time [12], [13]. There are two important design changes in samples B and C: optimized quantum well/barrier thicknesses, and the addition of a novel dual-integrated waveguide-depletion layer, which consists of an electron collection layer simultaneously used as a passive waveguide core.

A schematic diagram of the dual-integrated waveguide-depletion layer is shown in Fig. 2. Light is fiber-coupled into the passive waveguide section and then guided into the active

Sample A

InGaAs, Be, 2.0 x 10^{19} cm^{-3}, 50 nm, *P+ contact layer*
Al$_{0.48}$In$_{0.52}$As, Be, 1.5 x 10^{18} cm^{-3}, 100 nm, *p+ contact layer*
7nm In$_{0.53}$Ga$_{0.47}$As/5nm GaAs$_{0.5}$Sb$_{0.5}$, u.i.d., 80 pairs, 960 nm, *absorption layer*
Al$_{0.235}$Ga$_{0.235}$In$_{0.53}$As, GaTe, 5.0 x 10^{18} cm^{-3}, 1000 nm, *N+ contact layer*
Al$_{0.329}$Ga$_{0.141}$In$_{0.53}$As, semi-insulating, 1000 nm, *waveguide rib layer*
Al$_{0.48}$In$_{0.52}$As, u.i.d., 50 nm, *stop layer*
Al$_{0.329}$Ga$_{0.141}$In$_{0.53}$As, semi-insulating, 1500 nm, *waveguide slab layer*
InP, *semi-insulating substrate*

Sample B

InGaAs, Be, 2.0 x 10^{19} cm^{-3}, 50 nm, *P+ contact layer*
Al$_{0.48}$In$_{0.52}$As, Be, 1.5 x 10^{18} cm^{-3}, 100 nm, *p+ contact layer*
5nm In$_{0.53}$Ga$_{0.47}$As/3nm GaAs$_{0.5}$Sb$_{0.5}$, u.i.d., 35 pairs, 280 nm, *absorption layer*
InGaAs, u.i.d., 1000 nm, *collection layer/waveguide core*
Al$_{0.48}$In$_{0.52}$As, GaTe, 5.0 x 10^{18} cm^{-3}, 1000 nm, *N+ contact layer*
InP, *semi-insulating substrate*

Sample C

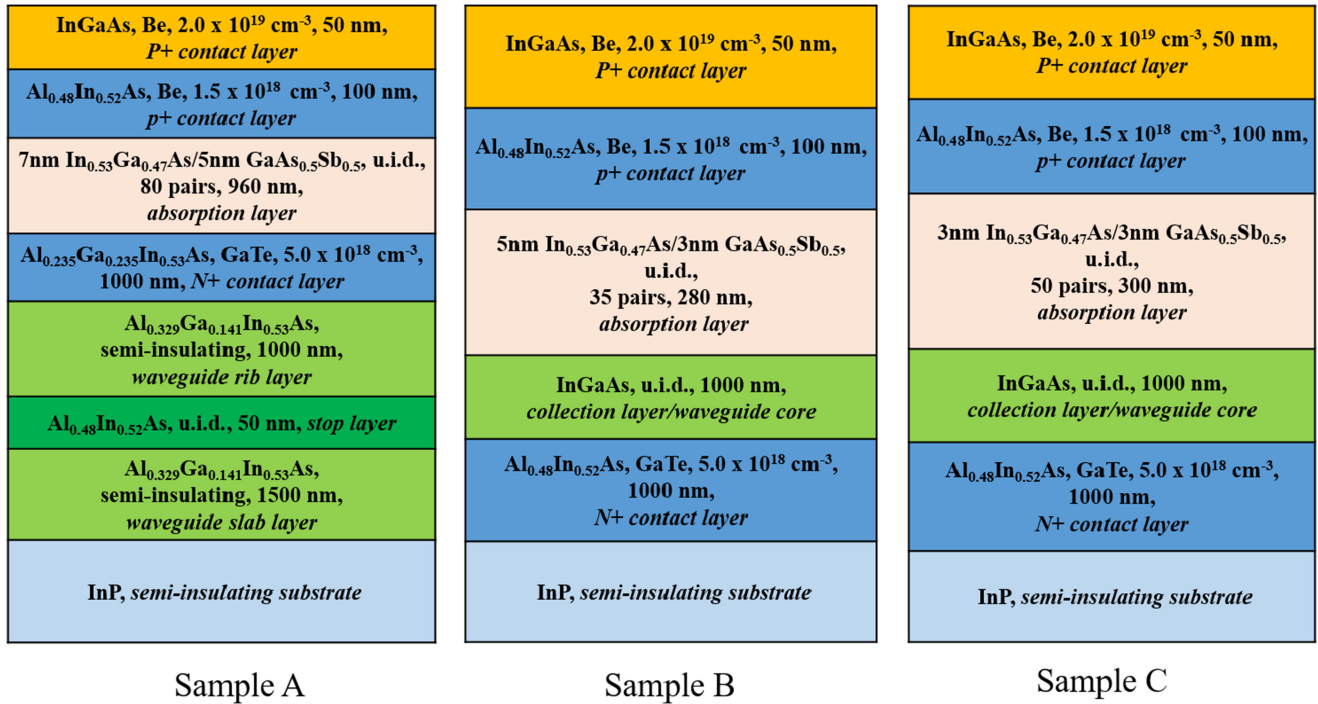| |
|---|
| InGaAs, Be, 2.0 x 10^{19} cm^{-3}, 50 nm, *P+ contact layer* |
| Al$_{0.48}$In$_{0.52}$As, Be, 1.5 x 10^{18} cm^{-3}, 100 nm, *p+ contact layer* |
| 3nm In$_{0.53}$Ga$_{0.47}$As/3nm GaAs$_{0.5}$Sb$_{0.5}$, u.i.d., 50 pairs, 300 nm, *absorption layer* |
| InGaAs, u.i.d., 1000 nm, *collection layer/waveguide core* |
| Al$_{0.48}$In$_{0.52}$As, GaTe, 5.0 x 10^{18} cm^{-3}, 1000 nm, *N+ contact layer* |
| InP, *semi-insulating substrate* |

Fig. 1.   InP-based type-II quantum well photodiodes structures in this study.
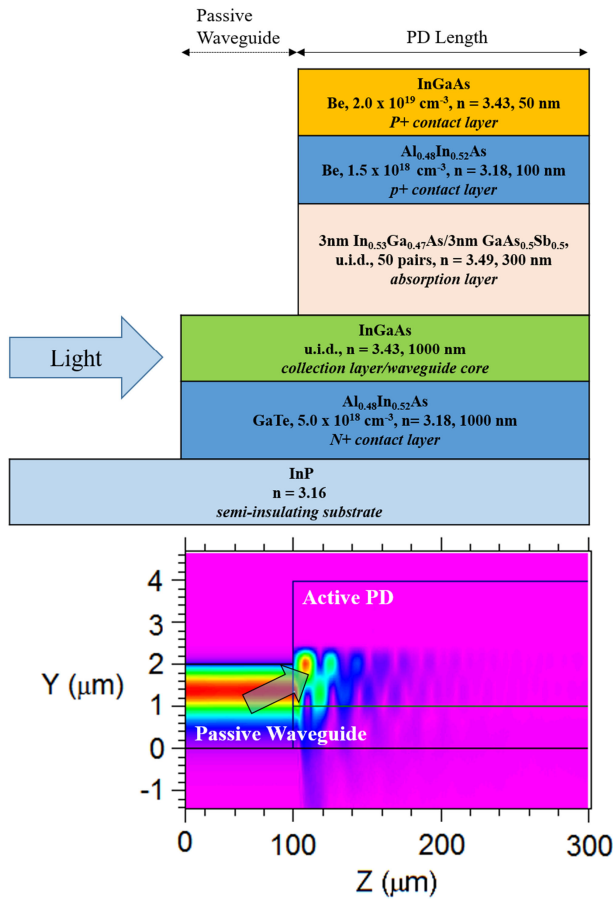

Fig. 2.   Schematic cross-sectional view of the PD. The light is coupled from the left into the passive waveguide, which couples light into the MQW absorption layer of the photodiode.

photodiode region, where it penetrates into the higher refractive index absorption layer. The light is absorbed, generating electron-hole pairs, with the electrons then being swept through the collection layer. The n-contact layer is made of a lower index material than the waveguide core layer in order to confine the optical mode within the waveguide core. The InGaAs waveguide core was designed to achieve a balance between the optical confinement factor within the waveguide and coupling loss from an optical fiber. The simulated confinement factor was 0.87 and the coupling loss from a lensed fiber was estimated to be about 7 dB. Since only a small portion of the mode propagates in the n-contact layer, free carrier absorption associated losses in the waveguide are negligible. This is in contrast to designs where a significant portion of the waveguide mode must propagate through the highly-doped contact region and potentially suffer from free-carrier absorption loss [5], [7].

Sample B includes 35 pairs of quantum wells with 5 nm thick InGaAs well layers and 3 nm thick GaAsSb barrier layers, and Sample C includes 50 pairs of quantum wells with 3 nm thick InGaAs well layers and 3 nm thick GaAsSb barrier layers. Samples B and C were designed with thinner quantum well and barrier layers than Sample A in order to increase the absorption efficient at 2 μm by enhancing the wave function overlap of electrons and holes, and, minimize the carrier escape time within the wells [14]. The band structure of the quantum wells and electron and hole wave functions were calculated using nextnano, a commercial device simulation software, and those within sample B are plotted in Fig. 3. One electron energy level exists in each InGaAs well, two heavy holes states and one light hole state exist in each GaAsSb hole well. In sample C, the InGaAs well is thinner than in Sample B leading to a shorter cut-off wavelength, as can be seen in the absorption coefficients
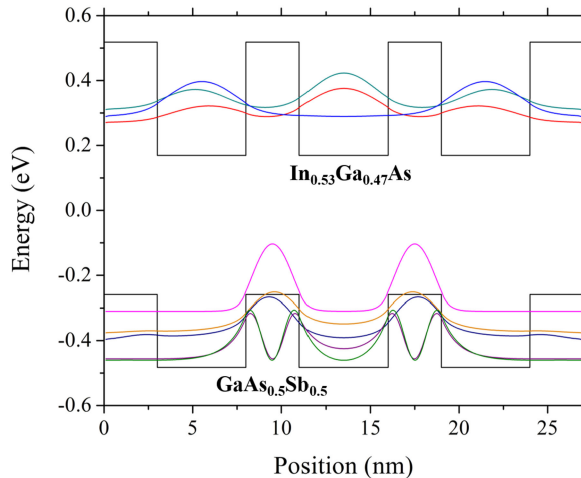
Fig. 3. Band structure and wave functions of Sample B. Green, red, and light blue curves represent electron wave functions of each well. Purple curve represents heavy hole wave functions. Orange and dark blue curves represent light hole wave functions in the ground state. Brown and green curves represent light hole wave functions in the second energy level.
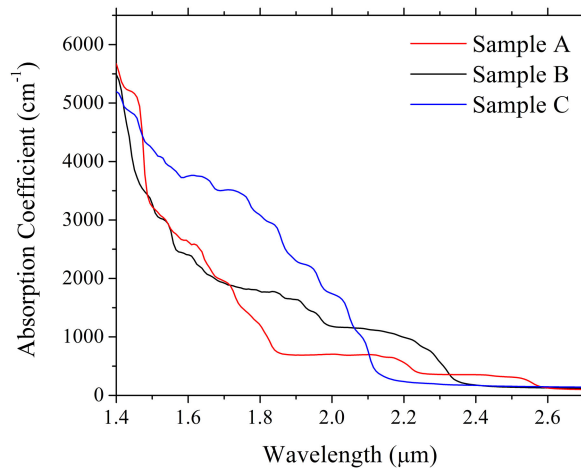

Fig. 4. Calculated absorption coefficients of samples A, B, and C.

shown in Fig. 4, which were calculated using the eight-band k·p method.

B. Device Fabrication

The device fabrication began with definition of different size active mesas using a MJB4 aligner. Ti/Pt/Au was deposited on top of the p-contact layer to provide an ohmic contact, followed by SiO_2 for surface passivation. Next, the mesas, along with 4 μm-wide, 1 μm-thick input rib waveguides, were etched with an Oxford Instruments Plasmalab-100 chlorine based ICP dry etching machine down to the semi-insulating substrate. Then, Au/AuGe/Pt/Ni was deposited on the n-mesa to provide an ohmic contact, followed by SU-8 as an insulation layer for coplanar waveguide (CPW) probe pads. A seed layer of Ti/Au was deposited and then electroplated to connect the CPW to the metal contacts.
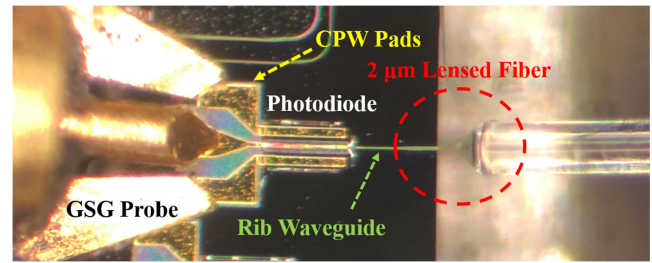

Fig. 5. Fabricated photodiode being measured with a microwave ground-signal-ground (GSG) probe and optically illuminated by a 2 μm laser through a lensed fiber.
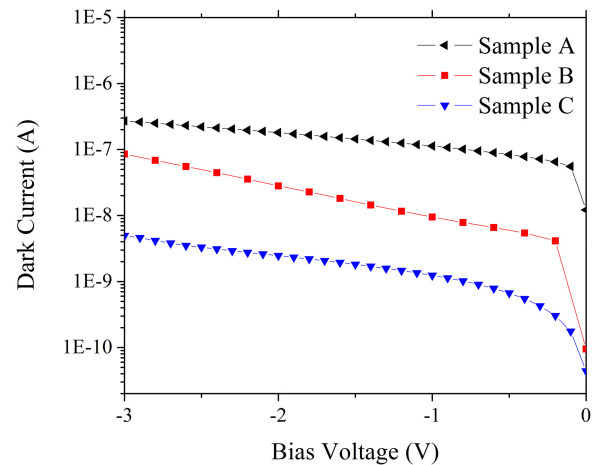

Fig. 6. Measured dark currents of 10 μm $\times$ 50 μm PDs fabricated from samples A, B, and C versus reverse bias.

III. RESULTS AND DISCUSSION

A. DC Measurements and Analysis

All the measurements were made at room temperature using on-wafer probing techniques as shown in Fig. 5. The measured photodiodes had dark currents ranging between 1 nA to 100 nA under -1 V bias. The dark current of photodiodes made from sample A is bulk-dominated and can be attributed to deep-level defects within the device [11]. Circular mesa photodiodes were also fabricated from Samples B and C, and the dark current of these devices were measured to be linearly dependent on the diameter of the mesa, suggesting that they are dominated by surface leakage. The dark currents of 10 μm $\times$ 50 μm devices fabricated from the three samples are shown in Fig. 6. Samples B and C show significant improvement in dark current due to their thinner MQW absorption regions and improved crystal quality.

The responsivity was measured for different sized devices on the three samples. A tapered fiber was used to butt-couple the input signal with 1.7-dBm optical power and a 2.5-μm diameter spot-size at 2-μm wavelength. The simulated and measured internal maximum responsivity of devices fabricated from all samples are plotted in Fig. 7. For a 20 μm $\times$ 200 μm device, the maximum internal responsivity observed at 2 μm was
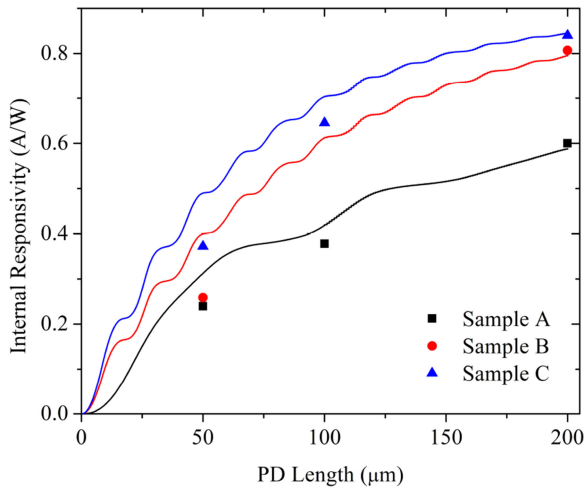
Fig. 7. Internal responsivity versus PD length. Solid curves represent simulated data and markers represent measured data at 5 V.
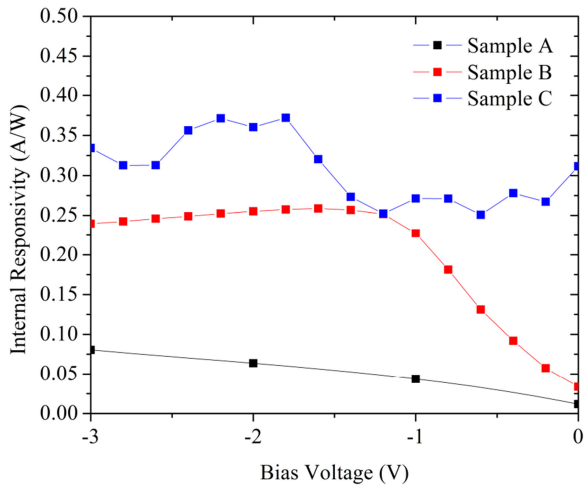

Fig. 8. Internal responsivity of 10 μm $\times$ 50 μm PDs fabricated from samples A, B, and C versus reverse bias.
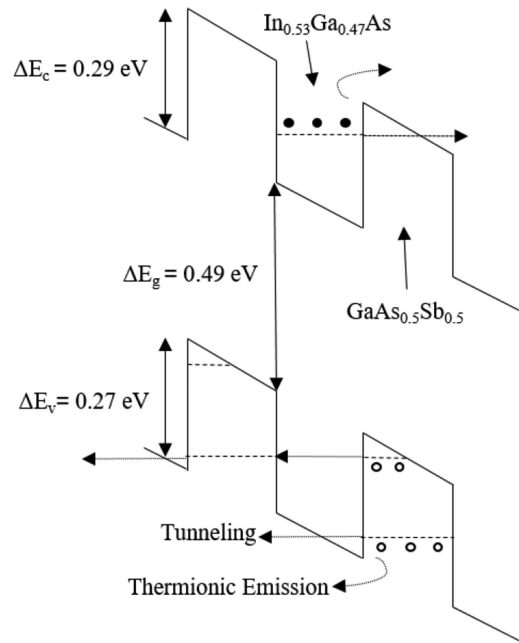

Fig. 9. Illustration of the carrier escape mechanisms in quantum wells.

mode beating occurs within the PDs and was optimized in the design of the PDs of samples B and C. In PDs made from sample A, the optical mode must couple through the n-contact layer before reaching the MQW absorption region. In contrast, when using the dual-integrated waveguide-depletion layer design, the optical mode is confined in the waveguide-depletion layer, and then coupled into the directly adjacent MQW absorption region within a shorter distance, enabling smaller devices and lower capacitances at a given responsivity. This can be seen in the rapid increase in internal responsivity of PDs made from samples B and C within the first 20 μm of the PD length, as shown in Fig. 7. Even though the PDs fabricated from samples B and C have thinner absorption layers, they achieve a higher internal responsivity than the PDs made from sample A due to the implementation of the dual-integrated waveguide-depletion layer and the increase in absorption coefficient. Furthermore, PDs made from sample C absorb more light at 2 μm than those made from sample B because they have a higher absorption coefficient and more quantum wells in the MQW absorption layer [14].

Fig. 8 shows the internal responsivity of 10 μm $\times$ 50 μm PDs fabricated from samples A, B, and C versus reverse bias. The responsivity increases with applied bias voltage because the depletion region widens and absorbs more light. Also, a larger applied electric field increases the electron and hole wavefunction overlap between the wells, which causes an increase of type-II absorption within the device [11].

B. High-Frequency Characteristics

In photodiodes with InGaAs/GaAsSb type-II quantum well absorption regions, the transit time is typically limited by the time it takes for photogenerated carriers to be swept out of the MQWs under the influence of an applied electric field, as illustrated in Fig. 9. Generally, there are two main physical mechanisms in which carriers escape from quantum wells: thermionic

0.6 A/W for sample A, 0.81 A/W for sample B, and 0.84 A/W for sample C. The absorption coefficients from Fig. 4 were used in the optical simulations, which were done in RSoft, a commercial beam propagation software. In order to calculate the internal quantum efficiency, we factored in the following loss mechanisms: fiber-chip coupling loss and reflection loss at the waveguide facet, as well as, free-carrier absorption in the waveguide, and carrier collection efficiency within the PD. Losses due to coupling and reflection were calculated to be 3.5 dB for sample A and 7 dB for samples B and C. Reflection losses can be mitigated by adding anti-reflection coating at the edge of the waveguide. The larger fiber coupling loss in devices made from samples B and C are due to a thin input waveguide thickness and can be improved with the integration of a spot-size converter [10]. The carrier collection efficiency of the PDs, which is limited by carriers that are trapped in the wells and recombine before reaching the contacts, is calculated to be 45% for Sample A and 55% for Samples B and C [11].

The measured responsivity increases with increasing photodiode length, as predicted in our optical simulations. Optical

emission and phonon-assisted tunneling [17]. Thermionic emission is the escape of carriers with a carrier thermal energy higher than the effective barrier height. The rate of thermionic emission of carriers is given by [19]

$$\tau_{therm,i} = \left(\frac{2\pi m_i L_w^2}{k_B T} \right)^{1/2} exp \left[\frac{\Delta E_b(F)}{k_B T} \right] \quad (1)$$

where m_i stands for effective mass in the wells, L_w represents the well thickness, T is the temperature, k_B is the Boltzmann constant, the subscript i can be e for electron, hh for heavy hole or lh for light hole, because the effective mass for electrons, heavy holes and light hole can differ [18]. $\Delta E_b(F)$ is the effective barrier height and can be expressed as

$$\Delta E_b(F) = E_\Gamma^{Barrier} - E_\Gamma^{Well} - \frac{qFL_w}{2} \quad (2)$$

and where F is the electric field, q is electron charge, and $E_\Gamma^{Barrier} - E_\Gamma^{Well}$ is the bulk band discontinuity between the well and barrier for electrons or holes. Tunneling is the escape of carriers through coherent, quantum mechanical tunneling of finite barriers and can be expressed as [17],

$$\tau_{tunnel,i} = \left(\frac{2m_i L_w^2}{\pi \hbar} \right)^{1/2} exp \left[\frac{2L_b \sqrt{2m_{bi} \Delta E_b(F)}}{\hbar} \right] \quad (3)$$

where L_b represents barrier thickness, m_{bi} stands for effective mass in barriers. This includes the tunneling of carriers out of a well into a neighboring well, and tunneling out of a well into continuum. Some carriers directly tunnel from quantum well to quantum well, with the assistance of a phonon, and can be trapped in the wells lower energy state before recombining through a localized defect, effectively reducing the collection efficiency of the device. However, we will only be considering tunneling of carriers into continuum as contributors to the photocurrent [15].

The total carrier transit time within the photodiode can be expressed as [18]

$$\tau_{transit,i} = n \left(\frac{1}{\tau_{therm,i}} + \frac{1}{\tau_{tunnel,i}} \right)^{-1} + \frac{n(L_w + L_b) + L_D}{v_i} \quad (4)$$

where n is the number of wells, L_D is the distance that an electron travels through the collection layer ($L_D = 0$ for holes), and v_i the carrier drift velocity in MQW layers. Short transit times can be achieved by reducing the effective barrier height and thickness of the wells, as well as, the number of quantum wells in the absorber layer.

In our case, we assume that only ground well state of electrons and holes are populated by photogenerated carriers because we measure the photodiodes with small optical power illumination at the wavelength used for measurement. We assume that electron-hole pairs are uniformly generated in the absorption region and that once carriers escape from a quantum well they then travel through continuum until reaching the electrode and contributing to the external photocurrent [15]. Due to their large effective mass, heavy holes are extremely slow and take a long time to escape from the quantum wells and,

therefore, are not considered to contribute to the photocurrent at high-frequencies. More specifically, the transit time of heavy holes is around 10 μs, which is comparable to the recombination time, so many of these carriers will recombine before they transit through the quantum wells to the electrodes and not contribute to the photocurrent, also reducing the collection efficiency of the device [18].

Electrons and light holes escape the wells at different rates due to their distinctive effective masses and bound energy levels within the wells. Electrons tunnel faster than light holes due to their smaller effective mass, however, light holes escape through thermionic emission at a faster rate because the effective energy barrier height of light holes is smaller than for electrons. The frequency response associated with the transit time of electrons or holes can be expressed as [16]

$$F_i(\omega) = \left| \frac{\sin \left(\frac{\omega \tau_{transit,i}}{2} \right)}{\frac{\omega \tau_{transit,i}}{2}} \right| \quad (5)$$

where ω is the angular frequency. The total transit time limited frequency response is determined by the combination of contributions of electrons and light holes.

The total frequency response of a p-i-n photodiode is determined by the product of the RC time constant and the total carrier transit time, and is expressed as [18]

$$H(\omega) = \frac{1}{1 + \frac{j\omega \tau_{transit}}{3.5}} \frac{1}{1 + j\omega(R_s + R_L)C_j} \quad (6)$$

where R_s is the series resistance, R_L is the load resistance, and C_j is the junction capacitance of the photodiode. For a 10 μm × 50 μm PD, R_s is 33 Ω and C_j is 0.1 pF, meaning the RC-limited 3-dB bandwidth is around 19 GHz.

To measure the bandwidth of the PDs, we used a 2 μm wavelength E-O Space intensity modulator to modulate a CW optical signal and an Agilent PSA Series E4440A electrical spectrum analyzer to measure the output RF power of the PDs. The measurements revealed a 3-dB bandwidth of 4.5 GHz for a 10 μm × 50 μm PD made from Sample B and a maximum 3-dB bandwidth above 10 GHz for a 10 μm × 50 μm PD made from Sample C at -3 V bias with 1.1 mW optical input power (Fig. 10). PDs from sample B are transit-time limited, as they are well below the RC-limited bandwidth. However, at this specific bias, PDs from sample C are RC-limited as the transit time limited bandwidth is calculated to be 37 GHz, which is nearly double the RC-limited bandwidth. Furthermore, the maximum 3-dB bandwidth of PDs made on Sample C can be made higher in the future by designing and fabricating smaller active area devices.

We also consider the dependence of an applied electric field across the MQW region [15]. These effects can be observed in the bandwidth measurements taken of a 10 μm × 50 μm PD made from Sample A shown in Fig. 11. At −7V, the bandwidth decreased from a maximum of 3.5 GHz (at −1 V) to 2.2 GHz. The bandwidth of these devices vary with applied bias, as the escape time of photogenerated electrons and holes in the wells vary. As can be seen in Fig. 12, light holes transit through the depletion region slower than electrons and limit the carrier transit time at high-frequencies. Therefore, two frequency roll-offs exist, one at low-frequency for light holes, and
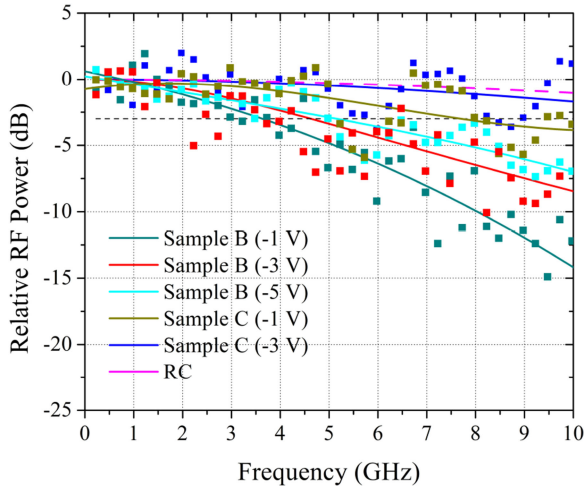
Fig. 10. Measured frequency response of 10 μm × 50 μm PDs fabricated from sample B and C at different bias voltages with 1.1 mW of optical input power. The dots represent measured data and the curves represent calculated data (Eq. (6)) and the RC-limited bandwidth of a 10 μm × 50 μm PD.
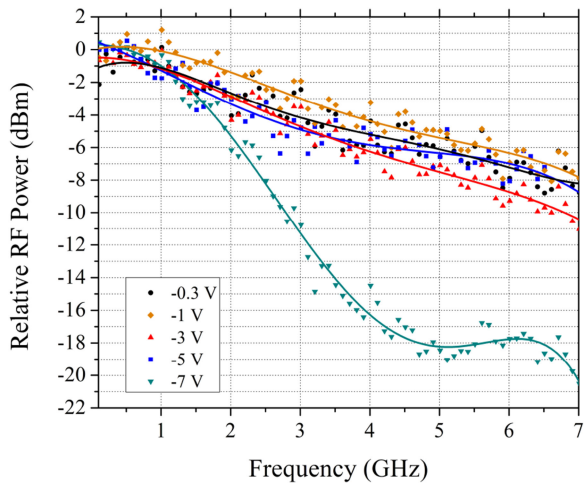

Fig. 11. Frequency response of a 10 μm × 50 μm PD fabricated from sample A under different bias voltages at an average photocurrent of 530 μA. Lines represent averaged data points.
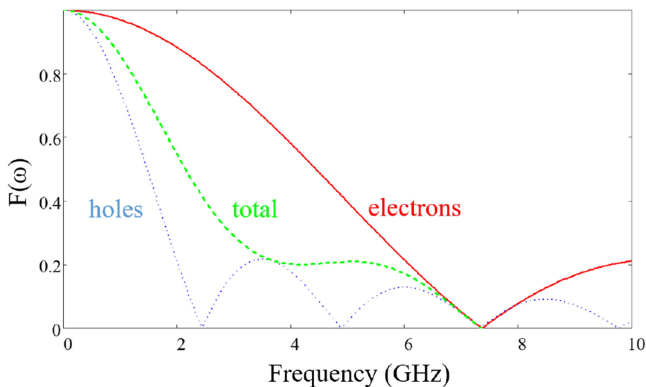

Fig. 12. Calculated frequency responses of electrons and light holes and total transit time limited frequency response of PDs made from Sample A biased at −7 V (calculated using Eq. (5) for electrons and light holes with values listed in Table I.)

TABLE I
PARAMETERS USED FOR FIGURE 12 (TAKEN FROM NEXTNANO)

Material	m_e	m_{lh}	L_w	L_b	$\Delta E_b(F)$
InGaAs	$0.041m_o$	$0.066m_o$	7 nm	5 nm	0.25 eV
GaAsSb	$0.0447m_o$	$0.052m_o$	5 nm	7 nm	0.18 eV

another one at high-frequency for electrons. The bandwidth in these PDs are lower than the PDs made from Samples B and C because the bound electron and hole energy levels are lower and the effective barrier heights are larger, leading to longer carrier escape times. At low biases, carrier escape is dominated by thermionic emission of carriers above the barriers [11]. Tunneling processes are suppressed due to the heavy effective masses of the electrons and holes. At high biases, carriers escape through the combination of thermionic emission and tunneling [20]. With a high applied electric field, the ground state energy levels of electrons and holes are lowered towards the bottom triangular section of the well [21]. We see a corresponding decrease in bandwidth with an increase in bias associated with the ground electron and hole energy levels lowering, resulting in longer carrier escape times. At a high enough applied electric field, the energy level will begin to rise again, and the carrier escape time will decrease, increasing the total bandwidth of the PD.

Fig. 13 shows electrical eye diagrams of a 10 μm × 50 μm PD made from sample C biased at -8 V and operating at 1, 5, and 10 Gbit/s. The bit pattern was generated by an Advantest D3186 Pulse Pattern Generator and connected to a RF signal generator and a 2 μm E-O space modulator with 10 GHz bandwidth, which modulates the incoming 3.5-dBm optical signal coming from a Thorlabs 2 μm Fabry-Perot laser diode that, subsequently, generates an optical eye bit pattern that is coupled into the photodiode. After probing the photodiode with a GGB high-speed GSG probe, the output of the PD was amplified by a RF amplifier (Gain = 30 dB, Saturation power = 20 dBm, Bandwidth = 40 GHz, Noise Figure = 6 dB) before electrical eye diagrams were measured using an Agilent Infiniium DCA-J 86100C sampling oscilloscope. Significant improvement of the eye opening at 10 Gb/s can be made by calibrating out the losses coming from the RF cables and the optical modulator, and by switching to a low noise amplifier (LNA). Furthermore, with implementation of advanced forward error correction (FEC) coding techniques, we expect that these devices can be used practically at 10 Gbit/s in a 2 μm optical communications system.

IV. CONCLUSION

In this paper, waveguide-integrated photodiodes (PDs) based on multiple InGaAs/GaAsSb type-II quantum wells (MQW) have shown capability of efficient high-speed detection at 2 μm. Through the modification of the quantum well and barrier thicknesses, and the addition of a novel dual-integrated

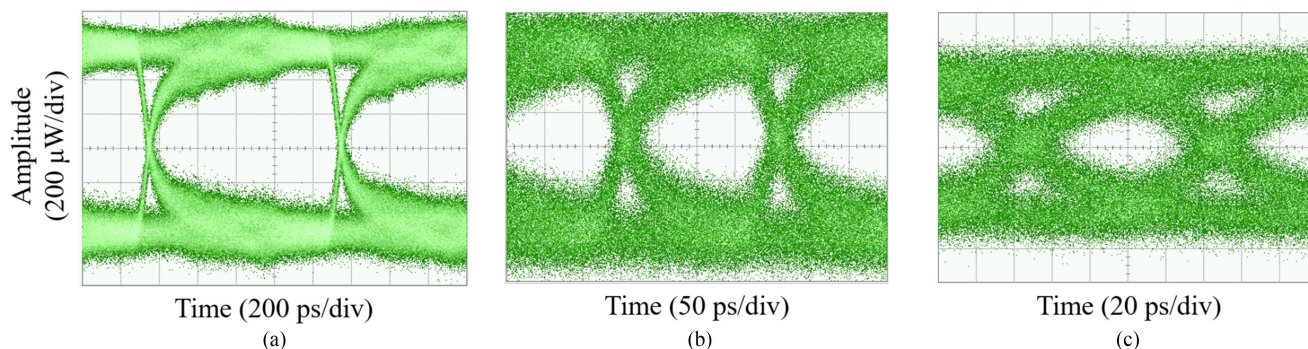Fig. 13.   Synthesized NRZ 16 bit eye pattern at (a) 1 Gb/s, (b) 5 Gb/s, and (c) 10 Gb/s at 2 μm wavelength by a 10 μm × 50 μm PD photodiode made on Sample C biased at −8 V.

waveguide-depletion layer, we have designed and fabricated photodiodes with a dark current as low as 1 nA at −1 V, a maximum internal responsivity of 0.84 A/W and a 3-dB bandwidth greater than 10 GHz at 2 μm. Open eye diagrams at 2 μm have also been measured at 1, 5, and 10 Gbit/s. The high-speed carrier dynamics of these photodiodes have been studied and explored for the first time, and reveal the high-frequency limits in the transit time associated frequency response being attributed to the carrier escape times of light holes in the quantum wells.

REFERENCES

[1] N. Ye *et al.*, "InP-based active and passive components for communication systems at 2 μm," *J. Lightw. Technol.*, vol. 33, no. 5, pp. 971–975, Mar. 2015.

[2] A. Spott, E. J. Stanton, N. Volet, J. D. Peters, J. R. Meyer, and J. E. Bowers, "Heterogeneous integration for mid-infrared silicon photonics," *IEEE J. Sel. Topics Quantum Electron.*, vol. 23, no. 6, Nov./Dec. 2017, Art. no. 8200810.

[3] P. J. Roberts *et al.*, "Ultimate low loss of hollow-core photonic crystal fibres," *Opt. Express*, vol. 13, no. 1, pp. 236–244, Jan. 2005.

[4] A. Joshi and D. Becker, "High-speed low-noise p-i-n InGaAs photoreceiver at 2-μm wavelength," *IEEE Photon. Technol. Lett.*, vol. 20, no. 8, pp. 551–553, Apr. 2008.

[5] B. Corbett *et al.*, "High speed AIInGaAs/InGaAs quantum well waveguide photodiode for wavelengths around 2 microns," in *Proc. Int. Conf. Indium Phosphide Related Mater.*, Aug. 2012, pp. 221–224.

[6] E. Ryckeboer *et al.*, "Silicon-on-insulator spectrometers with integrated GaInAsSb photodiodes for wide-band spectroscopy from 1510 to 2300 nm," *Opt. Express*, vol. 21, no. 5, pp. 6101–6108, Mar. 2013.

[7] R. Wang *et al.*, "2 μm wavelength range InP-based type-II quantum well photodiodes heterogeneously integrated on silicon photonic integrated circuits," *Opt. Express*, vol. 23, no. 20, pp. 26834–26841, Oct. 2015.

[8] S. W. Henderson *et al.*, "Coherent laser radar at 2 μm using solid-state lasers," *IEEE Trans. Geosci. Remote Sens.*, vol. 31, no. 1, pp. 4–15, Jan. 1993.

[9] T. F. Refaat *et al.*, "Backscatter 2-μm lidar validation for atmospheric CO_2 differential absorption lidar applications," *IEEE Trans. Geosci. Remote Sens.*, vol. 49, no. 1, pp. 572–580, Jan. 2011.

[10] A. Umbach, D. Trommer, R. Steingruber, A. Seeger, W. Ebert, and G. Unterborsch, "Ultrafast, high-power 1.55 μm side-illuminated photodetector with integrated spot size converter," in *Proc. Opt. Fiber Commun. Conf.*, vol. 4, Mar. 2000, pp. 117–119.

[11] B. Tossoun *et al.*, "High-speed InP-based p-i-n photodiodes with InGaAs/GaAsSb type-II quantum wells," *IEEE Photon. Technol. Lett.*, vol. 30, no. 4, pp. 399–402, Feb. 2018.

[12] F. J. Effenberger and A. M. Joshi, "Ultrafast, dual-depletion region, InGaAs/InP p-i-n detector," *J. Lightw. Technol.*, vol. 14, no. 8, pp. 1859–1864, Aug. 1996.

[13] C. L. Daunt *et al.*, "Sub 10 ps carrier response times in electroabsorption modulators using quantum well offsetting," *IEEE J. Quantum Electron.*, vol. 48, no. 11, pp. 1467–1475, Nov. 2012.

[14] B. Chen, W. Sun, J. C. Campbell, and A. L. Holmes, "Quantum efficiency modeling of PIN photodiodes with InGaAs/GaAsSb quantum wells absorption region," in *Proc. Photon. Conf.*, 2011, pp. 35–36.

[15] B. Chen and A. L. Holmes, Jr., "Carrier dynamics in InP-based PIN photodiodes with InGaAs/GaAsSb type-II quantum wells," *J. Phys. D, Appl. Phys.*, vol. 46, no. 31, 2013, Art. no. 315103.

[16] G. Lucovsky, R. F. Schwarz, and R. B. Emmons, "Transit-time considerations in p-i-n diodes," *J. Appl. Phys.*, vol. 35, no. 3, pp. 622–628, Aug. 1963.

[17] M. A. Fox, D. A. Miller, G. Livescu, J. E. Cunningham, and W. Y. Jan, "Quantum well carrier sweep out: Relation to electroabsorption and exciton saturation," *IEEE J. Quantum Electron.*, vol. 27, no. 10, pp. 2281–2295, Oct. 1991.

[18] G. Zhou and P. Runge, "Modeling of multiple-quantum-well p-i-n photodiodes," *IEEE J. Quantum Electron.*, vol. 50, no. 4, pp. 220–227, Apr. 2014.

[19] D. J. Moss, T. Ido, and H. Sano, "Calculation of photogenerated carrier escape rates from GaAs/$Al_xGa_{1-x}As$ quantum wells," *IEEE J. Quantum Electron.*, vol. 30, no. 4, pp. 1015–1026, Apr. 1994.

[20] S. Goswami, L. Davis, and P. K. Bhattacharya, "Temporal response of photodiodes with GaAs/$Al_xGa_{1x}As$ (0.1 × 0.3) multiquantum well absorption regions," *J. Appl. Phys.*, vol. 72, no. 10, pp. 4888–4892, Jul. 1992.

[21] A. P. Boltaev, N. N. Loiko, M. M. Rzaev, and N. N. Sibeldin, "External electric field effect on energy level positions in a quantum well," Russian Acad. Sci., Lebedev Phys. Inst., Moscow, Russia, Tech. Rep. QW/SL.06P, Jun. 2000.

Authors' biographies not available at the time of publication.